

# DWGS: Enhancing Sparse-View Gaussian Splatting with Hybrid-Loss Depth Estimation and Bidirectional Warping

Yu Ma, Guoliang Wei, Yue Cheng

arXiv:2509.24893v1 [cs.CV] 29 Sep 2025

**Abstract**—Novel View Synthesis (NVS) from sparse views remains a core challenge in 3D reconstruction, typically suffering from overfitting, geometric distortion, and incomplete scene recovery due to limited multi-view constraints. Although 3D Gaussian Splatting (3DGS) enables real-time, high-fidelity rendering, it suffers from floating artifacts and structural inconsistencies under sparse-input settings. To address these issues, we propose DWGS, a novel unified framework that enhances 3DGS for sparse-view synthesis by integrating robust structural cues, virtual view constraints, and occluded region completion. Our approach introduces three principal contributions: a Hybrid-Loss Depth Estimation module that leverages dense matching priors with reprojection, point propagation, and smoothness constraints to enforce multi-view consistency; a Bidirectional Warping Virtual View Synthesis method generates virtual training views to impose stronger geometric and photometric constraints; and an Occlusion-Aware Reconstruction component that utilizes depth-difference mask and a learning-based inpainting model to recover obscured regions. Extensive experiments on standard benchmarks—LLFF, Blender, and DTU—show that DWGS achieves a new state-of-the-art, achieving up to 21.13 dB PSNR and 0.189 LPIPS, while retaining real-time inference capabilities. Code is available at: <https://github.com/eternalland/DWGS>.

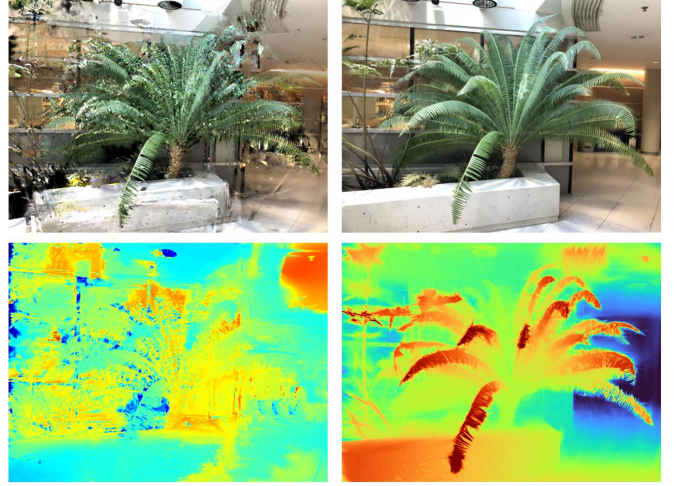
**Index Terms**—Novel View Synthesis, Sparse Views, 3D Gaussian Splatting, Depth Estimation, Bidirectional Warping

## I. INTRODUCTION

**N**OVEL View Synthesis (NVS) aims to generate realistic 3D scenes from 2D images, serving as a cornerstone for applications in virtual reality [1], robotics [2], and autonomous driving [3]. While Neural Radiance Fields (NeRF) [4] achieve photorealistic quality through implicit neural modeling, they require dozens of input views and suffer from high computational costs, hindering real-time use. 3D Gaussian Splatting (3DGS) [5] emerged as an efficient explicit alternative, leveraging optimizable Gaussians and differentiable rasterization for high-fidelity, real-time rendering. However, under sparse-view conditions (e.g., 3–5 images), insufficient multi-view constraints cause 3DGS to overfit, leading to geometric distortions, floating artifacts, background collapse, and incomplete occlusion handling, especially in complex 360° scenes.

NVS under sparse-view conditions primarily grapples with three fundamental challenges: (1) Inadequate Geometry Initialization: Vanilla 3DGS relies on COLMAP-generated sparse point clouds for initializing Gaussian primitives. Under sparse inputs, these points become insufficient and noisy, failing to support meaningful Gaussian reconstruction. This often causes primitives to over-scale in an attempt to cover surrounding regions, rather than densify appropriately through cloning or

Y.Ma, G.Wei, Y.Cheng, University of Shanghai for Science and Technology,  
E-mail: yummychina@163.com



(a) Rendered image and depth map comparison between 3DGS and DWGS.



(b) Training Efficiency vs. Rendering Quality.

Fig. 1. (a) 3DGS outputs (left) vs. DWGS outputs (right) for both image and depth map. (b) presents an efficiency-quality scatter plot comparing DWGS with various baseline methods.

splitting under sparse conditions, resulting in blurry and unstable geometry. (2) Under-Constrained Optimization: Limited training views provide weak supervisory signals, leading to overfitting and poor generalization. The model often produces floaters and inconsistent geometry when rendered from novel poses. (3) Occlusion and Unseen Regions: Areas unobserved in all training views cannot be recovered without strong priors or explicit reasoning, resulting in holes or incorrect content in disoccluded regions.

To address the challenges of sparse-view NVS, recent studies have proposed various approaches [6]–[11]. NeRF-

based methods mitigate overfitting through depth regularization, semantic consistency, and pre-trained priors, but they remain constrained by long training times and slow inference. 3DGS-based methods exploit the flexibility of explicit representations, exploring depth-guided optimization, multi-view consistency constraints, and diffusion model priors, significantly improving efficiency and quality. For instance, depth regularization methods [11] provide geometric priors via monocular depth estimation or Multi-View Stereo (MVS) with virtual view generation and co-regularization enhance multi-view consistency. Nevertheless, existing methods still face limitations in geometric consistency, occlusion handling, and detail recovery under sparse views, particularly in complex scenes, where scale inconsistencies in monocular depth priors and low overlap in MVS can lead to inaccurate geometry.

To tackle these challenges, we propose DepthWarpGS (DWGS), a novel 3DGS-based framework designed for high-quality and efficient novel view synthesis from sparse input views. The framework introduces three key innovations: First, a Hybrid-Loss Depth Estimation module utilizes a dense matcher to extract sufficient initialization points, followed by a novel composite loss integrating reprojection error, point propagation, and Total Variation (TV) smoothness constraints to obtain robust depth estimates, significantly enhancing multi-view consistency. The point propagation constraint specifically strengthens geometric consistency by exploiting indirect correspondences across multiple views (e.g., deriving constraints between points  $a$  and  $c$  via their common matches to point  $b$  in overlapping images). Second, a Bidirectional Warping Virtual View Synthesis strategy is employed to generate photometrically and geometrically consistent virtual views, providing additional supervision signals to improve robustness. Third, an Occlusion-Aware Reconstruction component addresses occlusion challenges through depth-difference-based foreground mask and a dedicated inpainting model, effectively reconstructing missing regions by prioritizing background content. Figure 1 presents a comparison between DWGS and other baseline methods.

The main contributions of this work are the following:

- A unified DWGS framework integrating depth estimation, virtual view synthesis, and occlusion processing for sparse-view 3DGS that achieves efficient NVS.
- A robust Hybrid-Loss Depth Estimation module is introduced, leveraging dense matching priors and enforcing multi-view geometric consistency through a composite loss that incorporates reprojection, point propagation, and Total Variation smoothness constraints.
- Bidirectional Virtual View Synthesis, a novel method that generates virtual training views using Bidirectional Warping. This approach imposes additional photometric and geometric constraints, significantly improving reconstruction quality.
- Occlusion-Aware Reconstruction, an innovative method is presented to effectively reconstruct heavily occluded regions. This is achieved through a depth-difference-based foreground mask mechanism and a dedicated inpainting model, which collectively prioritize the rendering of background content.

Extensive experiments on LLFF, IBRNet, Blender, DTU, and Tanks&Temples show that DWGS achieves new state-of-the-art performance across metrics including PSNR (up to 21.13dB) and LPIPS (as low as 0.189), while maintaining real-time rendering speeds. The framework demonstrates remarkable robustness across a spectrum of settings, from forward-facing to 360° scenes.

## II. RELATED WORKS

1) *NeRF-Based NVS Methods*: Neural Radiance Fields (NeRF) [4] implicitly represent scenes via Multi-Layer Perceptrons (MLPs), achieving photorealistic NVS through volume rendering and becoming a dominant approach in recent years. Subsequent improvements include Mip-NeRF [12], which mitigates aliasing via conical frustum rendering; Mip-NeRF360 [13], extending the framework to 360° unbounded scenes; and InstantNGP [14], which reduces training time to seconds using multi-resolution hash encoding. However, these methods generally require dense view inputs (often dozens of images) and suffer from slow training and inference. Moreover, in sparse-view settings, NeRF-based approaches are prone to overfitting, resulting in blurry or inconsistent novel views.

To address sparse-view challenges, various regularization strategies have been proposed. RegNeRF [15] mitigates overfitting with color and depth consistency regularization for unseen views, DietNeRF [6] enforces semantic consistency using CLIP [16] embeddings, and SparseNeRF [7] enhances geometry with scale-invariant losses from monocular depth estimation. ViP-NeRF [17] and FreeNeRF [8] improve training stability via visibility regularization and frequency control, respectively. ReconFusion [18] integrates diffusion models to generate additional views while struggling with view consistency. Pose-free reconstruction methods like iNeRF [19], NeRFmm [20], and BARF [21] jointly optimize camera poses and scene representations but are limited under complex camera trajectories (e.g., 360° scenes). These methods rely on volume rendering, resulting in low efficiency unsuitable for real-time applications.

2) *3DGS-Based NVS Methods*: 3DGS represents scenes with explicit Gaussian primitives, achieving real-time rendering via differentiable rasterization, surpassing NeRF in efficiency and quality. 3DGS excels with dense views, supporting tasks like text-to-3D generation [22], [23] and dynamic scene modeling [24], [25]. However, in sparse views, 3DGS suffers from insufficient initial point clouds and limited multi-view constraints, leading to floating artifacts and geometry degradation.

Recent studies optimize sparse-view 3DGS with various strategies. FSGS [26] enhances geometry via unpooling and monocular depth priors but suffers from long training times, limiting its applicability in time-sensitive scenarios. GaussianObject [10] proposes structure-prior-aided initialization, needing only 4 views, and uses diffusion models to repair occluded regions. DNGaussian [27] optimizes Gaussian positions with global-local depth normalization, addressing scale inconsistencies. CoherentGS [28] enhances Gaussian consistency

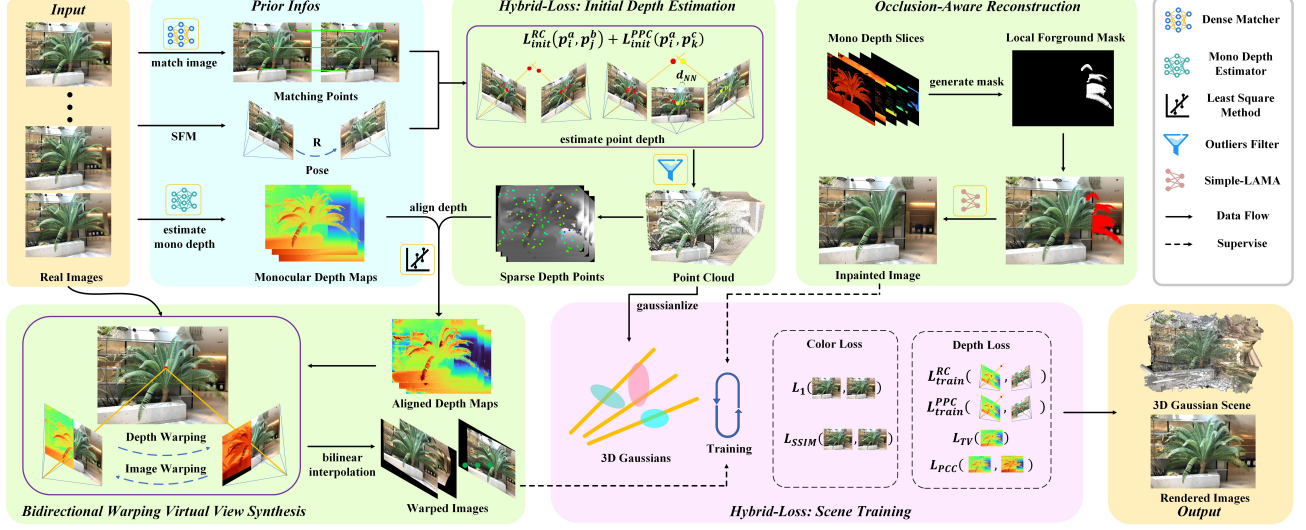


Fig. 2. DWGS Pipeline. Sparse images are processed via dense matching, structure from motion (SfM), and monocular depth estimation to obtain correspondences, poses, and depth maps. These are fused in a Hybrid-Loss module for robust point-wise depth. Point cloud depths are aligned with monocular depth maps using least-squares optimization to recover scale. Aligned depths and images undergo Bidirectional Warping and interpolation to produce warped images. Occlusion-Aware Reconstruction utilizes an inpainting model (Simple-LAMA) to restore occluded background regions. The 3D Gaussian scene is reconstructed by optimizing a combined loss function comprising color loss and depth loss.

using an implicit decoder and smoothness loss, filling occluded regions. CoR-GS [29] suppresses Gaussian field disagreements via co-regularization, improving geometric consistency. LM-Gaussian [30] integrates stereo priors [31] and diffusion models [32] for iterative detail refinement. MVPGS [33] leverages MVS [34] and Vision Transformers (ViTs) [35] to excavate multi-view cues, optimizing initialization and appearance. MCGS [36] introduces a sparse matcher and progressive pruning for multi-view consistency. SCGaussian [37] introduces a hybrid Gaussian representation with structure-consistent optimization and matching priors to enhance 3D consistency. Binocular-Guided 3DGS [38] constrains rendered depths with binocular stereo consistency, improving view consistency. SID [39], as an enhanced version of FSGS, incorporating semantic regularization from DINO-ViT [40] features and local depth constraints. While existing methods have made progress in specific areas, fundamental challenges including monocular depth scale inconsistencies, robust occlusion handling, and high-fidelity detail recovery in complex scenes remain largely open.

Our DWGS method presents a unified approach for high-quality sparse-view synthesis, integrating three core technical contributions that advance beyond previous methods. DWGS leverages dense matching to establish reliable correspondences, while maintaining training efficiency without Gaussian inflation as in FSGS [26]. The proposed Hybrid-Loss Depth Estimation incorporates multi-view geometric constraints and point propagation, offering stronger robustness than SCGaussian [37], which relies only on reprojection error. The Bidirectional Warping method produces more complete virtual views compared to the forward warping used in MVPGS [33], avoiding hole-filling and post-inpainting. Furthermore, the Occlusion-Aware Reconstruction module performs consistent occlusion handling within a single training stage, unlike

the complex two-stage diffusion-based refinement in LM-Gaussian [30]. The unified framework jointly addresses depth, consistency, and occlusion challenges under extreme sparsity, demonstrating clear improvements in rendering quality and operational efficiency.

### III. METHODS

The innovative methods employed in DWGS are introduced as follows: III-A. Preliminaries outlines the 3DGS fundamentals. III-B. Dense matching for sufficient initialization, ray-based 3DGS Optimization reduces degrees of freedom to prevent overfitting. III-C. Hybrid-Loss Depth Estimation improves geometric consistency via hybrid loss fusion. III-D. Bidirectional Warping generates virtual views to enhance photometric and geometric constraints. III-E. Occlusion-Aware Reconstruction handles occlusions using depth-difference mask and inpainting model. Figure 2 illustrates the pipeline of the proposed DWGS framework.

#### A. Preliminary for 3D Gaussian Splatting

DWGS leverages 3DGS [5] to represent 3D scenes with explicit Gaussian primitives, enabling real-time NVS through differentiable rasterization. Each Gaussian primitive is defined by a set of differentiable parameters: position vector  $\mu$ , rotation quaternion  $q$ , scaling matrix  $s$ , opacity  $\alpha$ , and spherical harmonic coefficients  $sh$  for view-dependent color, denoted as  $\mathcal{G} = \{G_i : \mu_i, q_i, s_i, \alpha_i, sh_i\}_{i=1}^P$ . The position and shape of each Gaussian follow a Gaussian distribution, formulated as:

$$G(x) = e^{-\frac{1}{2}(x-\mu)^T \Sigma^{-1}(x-\mu)}. \quad (1)$$

To ensure the covariance matrix  $\Sigma$  is positive semi-definite, it is decomposed into a scaling matrix  $s$  and a rotation

matrix  $R$  represented by quaternion  $q$ , reducing optimization complexity:

$$\Sigma = RSS^T R^T. \quad (2)$$

For projection into the image plane, the view transformation matrix  $W$  and the projective transformation Jacobian  $J$  are applied to map the 3D Gaussian as follows:

$$\Sigma' = JW\Sigma W^T J^T. \quad (3)$$

Pixel color  $C$  is computed via volume rendering, blending  $N$  ordered overlapping Gaussians:

$$C = \sum_{i \in N} c_i \alpha_i \prod_{j=1}^{i-1} (1 - \alpha'_j), \quad (4)$$

where  $c_i$  is the color of the  $i$ -th Gaussian.  $\alpha'_j = \alpha_j G(P)$  is derived from the projected 2D Gaussian  $\Sigma'$ . Pixel depth  $D$  is similarly computed:

$$D = \sum_{i \in N} d_i \alpha_i \prod_{j=1}^{i-1} (1 - \alpha'_j), \quad (5)$$

where  $d_i$  is the depth of the  $i$ -th Gaussian.

### B. Dense Matching and Ray-Based Gaussian Splatting

Vanilla 3DGS relies on sparse 3D points from COLMAP, which become critically insufficient under sparse-view conditions, leading to initialization failure and overfitting. To address this, two core prior enhancements are introduced.

**Dense Matching for Sufficient Initialization:** The standard sparse feature matching in COLMAP is replaced with a dense matching network. By leveraging inter-image correlations rather than independently extracted feature points, this approach produces denser and more reliable correspondences, significantly improving the quality and coverage of the initial 3D point cloud for Gaussian reconstruction.

**Ray-Constrained Optimization:** Gaussian centers are constrained to lie along camera rays, reducing 3D position optimization to a one-dimensional depth adjustment. Each point is parameterized as  $r = o + z \cdot d$ , where  $o$  is the optical center,  $d$  is the viewing direction, and  $z$  is the depth. This constraint enhances optimization stability, suppresses floating artifacts, and improves convergence, particularly under limited views.

### C. Hybrid-Loss Depth Estimation

Accurate depth estimation is crucial for high-quality scene reconstruction, as it provides the essential geometric information lacking in 2D imagery. However, under sparse-view conditions, the lack of strong multi-view constraints makes high-precision depth estimation difficult through reprojection error minimization alone. To improve depth reliability and multi-view consistency, a hybrid-loss module is proposed that integrates multiple geometric constraints. Figure 3 illustrates the pipeline of the Hybrid-Loss Depth Estimation module.

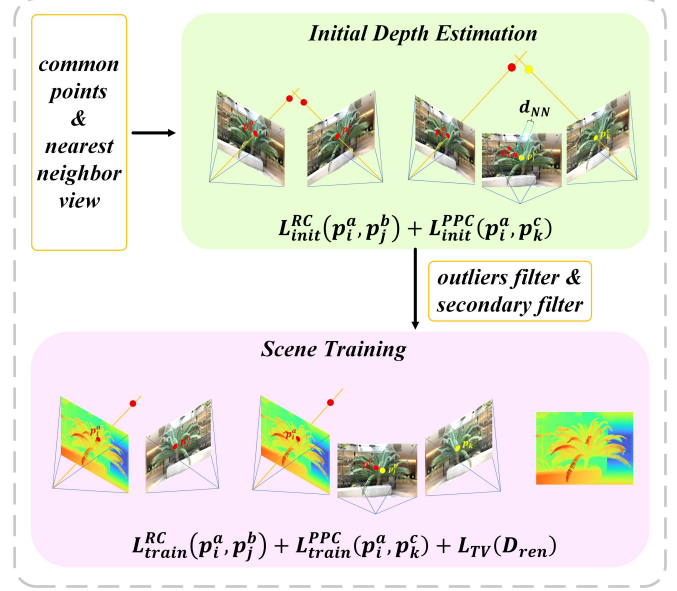


Fig. 3. Hybrid-Loss Depth Estimation pipeline, which first estimates initial point depth from densely matched points using reprojection and point propagation constraints, then filters outliers. During scene training, rendered depth is refined under reprojection, point propagation, and TV smoothness constraints. Point propagation constraint are computed from the common points. Nearest-neighbor view and secondary filter reducing redundant computation.

1) **Initial Depth Estimation Stage:** The depth estimation incorporates two geometric constraints and an outlier filtering mechanism as follows:

**Reprojection Constraint (RC):** Using dense image matching correspondences, such as point pair  $a-b$  between image pair  $I-J$ , point  $a$  from image  $I$  is back-projected into 3D space to obtain point  $A$ , which is then projected into image  $J$  to yield  $a'$ . The reprojection loss minimizes the Euclidean distance between the reprojected and original points  $a'-b$ :

$$L_{init}^{RC} = \sum_{i,j} \|\pi(K, R_{ij}, Ray(p_i^a, z_i^a)) - p_j^b\|_2^2, \quad (6)$$

where  $p_i$  and  $p_j$  are matching image points,  $K$  is the camera intrinsic,  $R_{ij}$  denotes the relative pose from view  $i$  to view  $j$ ,  $Ray(\cdot)$  denotes the ray function that generates spatial points, and  $\pi(\cdot)$  denotes the projection function.

**Point Propagation Constraint (PPC):** Unlike sparse matcher that independently extract feature points, dense matcher generate matching points based on image pairs, making reprojection error constraints alone insufficient for ensuring depth consistency and robustness. To address this, the Point Propagation Constraint is introduced: for matching point pair  $a-b$  between image  $I-J$ , and  $b'-c$  between image pair  $J-K$ , we use point  $b$  and  $b'$  in image  $J$  as a **bridge** to establish indirect geometric consistency between  $a$  and  $c$  across views. The common point set  $\mathcal{C}$  is defined as:

$$\mathcal{C}(p_i^a, p_k^c) = \begin{cases} (p_i^a, p_j^b) \in \mathcal{M}_{i,j}, \\ (p_j^b, p_k^c) \in \mathcal{M}_{j,k}, \\ \|p_j^b - p_j^{b'}\| < d_{NN}, \end{cases} \quad (7)$$

where  $\mathcal{M}_{i,j}$  denotes matched point pairs between images  $I$  and  $J$ , and  $d_{NN}$  is a mutual nearest-neighbor distance threshold. Since identical physical points may not align exactly in pixel coordinates, a mutual nearest-neighbor search is performed in a KD-Tree: for each  $p_j^b$ , its nearest neighbor  $p_j^{b'}$  is identified, and vice versa. If the distance between them is less than  $d_{NN}$ , they are considered the same point. The point propagation loss, similar to reprojection loss is formulated as:

$$L_{init}^{PPC} = \sum_{i,k} \|\pi(K, R_{ik}, Ray(p_i^a, z_i^a)) - p_k^c\|_2^2, \quad (8)$$

where  $R_{ik}$  denotes the relative pose from view  $i$  to view  $k$ , see appendix algorithm A for details.

**Outlier Filtering Mechanism:** Mismatched pairs on object edges can have low reprojection error yet high depth differences, whereas those in untextured areas may have low depth differences but high reprojection error. Hence, the Outlier Filtering Mechanism jointly considers both metrics for the Reprojection Constraint:

$$\begin{cases} \tau_{dy} = \tau_{base} + \alpha \cdot \text{Sigmoid}(2\hat{z} - 1), \\ M_{i,j}^{depth} = \frac{|z_{ij} - z_{ji}|}{\min(z_{ij}, z_{ji})} \leq \tau_{dy}, \\ M_{ij}^{error} = E_{ij}^{RC} \leq \tau_{RC}, \\ M_{i,j}^{RC-dep} = M_{ij}^{error} \odot M_{ji}^{error} \odot M_{i,j}^{depth}, \end{cases} \quad (9)$$

where the dynamic threshold  $\tau_{dy}$  is implemented using a Sigmoid function to enforce stricter depth consistency constraints for nearby points and more relaxed tolerances for distant points;  $\tau_{base}$  denotes the base threshold,  $\alpha$  is a scaling factor, and  $\hat{z}$  represents the normalized depth value;  $z_{ij}$  denotes the ray depth of image  $I$  in the image pair  $I-J$ ;  $M_{i,j}^{depth}$  is the depth consistency mask, obtained by comparing the relative depth difference with  $\tau_{dy}$ ;  $E_{ij}^{RC}$  denotes the reprojection error between images  $I$  and  $J$ ;  $\tau_{RC}$  is a fixed reprojection error threshold;  $M_{ij}^{error}$  is the reprojection error mask;  $M_{i,j}^{RC-dep}$  is the final valid matching mask that combines bidirectional reprojection errors and depth consistency. Based on this mechanism, matched point pairs are filtered if either the reprojection error exceeds the predefined threshold or the relative depth difference is too large.

The same filtering principle is extended to multi-view chains for the Point Propagation Constraint. The co-visible point set through the bridge view  $j$  is filtered as:

$$\begin{cases} M_{jik}^{PPC} \leftarrow \mathcal{C}(p_i^a, p_k^c), M_{i,k}^{depth} \leftarrow \mathcal{D}(z_{ij}, z_{kj}), \\ M_{jik}^{PPC-dep} = M_{jik}^{PPC} \odot M_{i,k}^{depth}, \end{cases} \quad (10)$$

where  $M_{jik}^{PPC}$  denotes the initial matching mask for the propagation path  $i \rightarrow j_{bridge} \rightarrow k$ , obtained from Eq. 7, and  $M_{i,k}^{depth}$  is obtained from Eq. 9.  $M_{jik}^{PPC-dep}$  represents the point propagation mask after applying depth-based filtering.

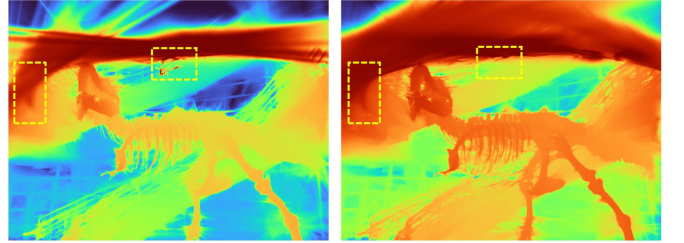
Additionally, two enhancement operations are applied: point propagation relations with a common point count below a predefined threshold are filtered out. In 360° unbounded scenes, point propagation relations are constructed based on the nearest-neighbor distances computed between different



(a) Matching points between two SCGaussian images.



(b) Matching points between two DWGS images.



(c) Depth map comparison after applying different outlier filtering methods between SCGaussian and DWGS.

Fig. 4. (a)(b) are the matching point maps of SCGaussian and DWGS, respectively. SCGaussian uses Ransac algorithm to filter outliers, while DWGS uses the Outlier Filtering Mechanism. Compared to SCGaussian, DWGS is more capable of removing outliers and retaining more valid points. (c) compares the depth maps of SCGaussian (left) and DWGS (right).

views. These two operations reduce unnecessary computations and significantly accelerate processing.

2) *Scene Training Stage:* In the scene training stage, we employ refined depth constraints, converting filtered matching points into spatial points and then into Gaussian primitives. To ensure robustness, the training stage includes three loss functions to constrain the rendered depth as follows:

**Reprojection & Point Propagation Constraint:** Inspired by SCGaussian [38], we apply Bilinear Sampling to the rendered depth map along rays, computing reprojection and point propagation errors from training views to other views to enforce spatial structure consistency.

$$\dot{p} = M \odot p \quad (11)$$

$$L_{train}^{RC} = \sum_{i,j} \|\pi(K, R_{ij}, Ray(\dot{p}_i^a, Bil(D_i))) - \dot{p}_j^b\|_2^2, \quad (12)$$

$$L_{train}^{PPC} = \sum_{i,k} \|\pi(K, R_{ik}, Ray(\dot{p}_i^a, Bil(D_i))) - \dot{p}_k^c\|_2^2, \quad (13)$$

where  $\dot{p}$  denotes the pixel point  $p$  after filtering, which is performed using either the mask  $M_{i,j}^{RC-dep}$  or  $M_{jik}^{PPC-dep}$ .  $D_i$  is the rendered depth map of view  $i$ ,  $\pi(\cdot)$  denotes the

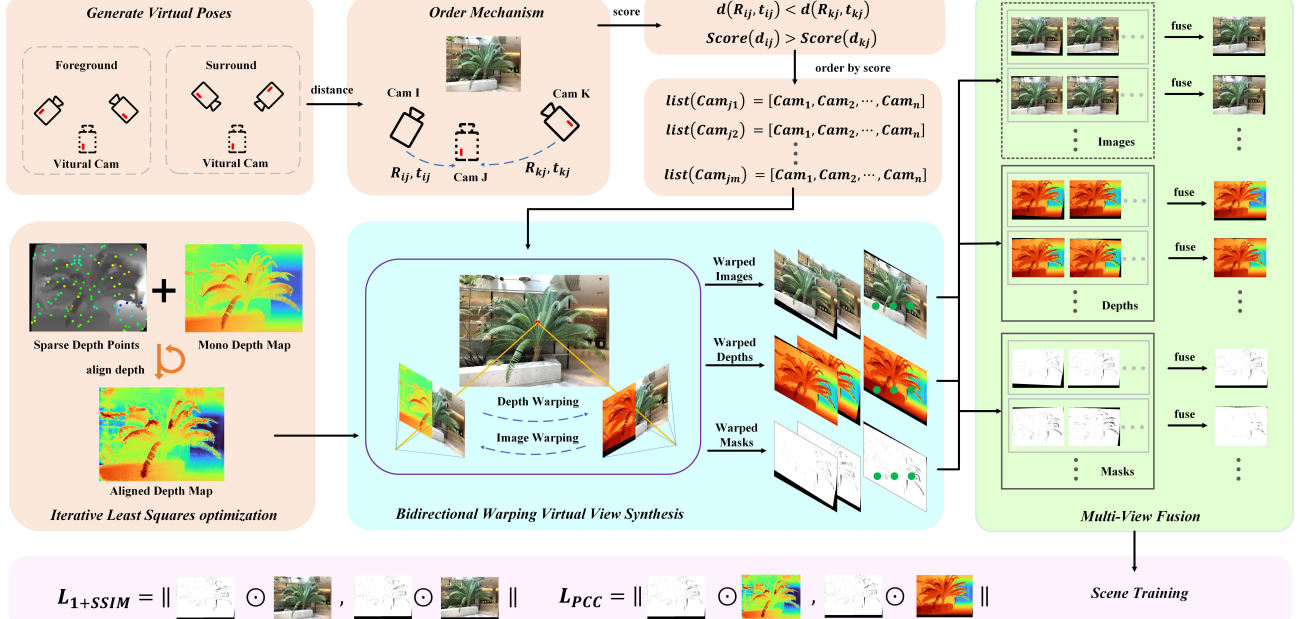


Fig. 5. Bidirectional Warping Virtual View Synthesis Pipeline. The monocular depth maps from the real views are aligned with sparse depth points via least-squares optimization. Depth Warping generates virtual depth maps, filling holes. Image Warping samples real views to create virtual views. Distance scores between real and virtual views are computed, warping multiple optimal real views to a single virtual view. The nearest-neighbor virtual view serves as the base for Multi-View Fusion. The 3D Gaussian scene is reconstructed using gradient-domain loss and Pearson Correlation Coefficient (PCC) loss constraints.

ray function that generates spatial points,  $\pi(\cdot)$  denotes the projection function,  $Bil(\cdot)$  denotes bilinear sampling.

**Smoothness Constraint:** Total Variation (TV) loss is applied to promote spatial smoothness in the rendered depth map.

$$L_{TV} = \sum_{u,v} (|\nabla_x D_i(u,v)| + |\nabla_y D_i(u,v)|) \quad (14)$$

where  $u, v$  are pixel coordinates,  $D_i$  is the rendered depth map of view  $i$ , and  $\nabla_x$  and  $\nabla_y$  denote the horizontal and vertical gradient operators, respectively.

The final depth loss functions for the Initial Depth Estimation Stage and the Scene Training Stage are defined as follows:

$$L_{init} = L_{init}^{RC} + L_{init}^{PPC}, \quad (15)$$

$$L_{train} = L_{train}^{RC} + L_{train}^{PPC} + L_{TV}. \quad (16)$$

Figure 4 presents a comparative visualization between the results without and with the Outlier Filtering Mechanism, along with a comparison of the depth maps generated after applying the Hybrid-Loss.

#### D. Bidirectional Warping Virtual View Synthesis

1) **Virtual View Generation Strategy:** In sparse-view scenarios, particularly with as few as 3 images, 3DGS rendering often suffers from overfitting and severe geometric distortions due to insufficient multi-view constraints, especially when input views are spatially clustered. To mitigate this, we propose generating multiple virtual views via Depth-Image-Based Rendering (DIBR) to impose stronger photometric and geometric constraints during 3DGS optimization. DIBR, also known as 3D Image Warping, is a core computer graphics technique that projects reference images into 3D space using depth maps

and reprojects 3D points onto a virtual camera's image plane. Two primary warping strategies exist: (1) Forward Warping, which is computationally simple but often produces holes and disocclusions, leading to less effective synthesis; and (2) Backward Warping, which provides higher-quality results but requires the depth map of the target view. Our approach integrates both strategies through Bidirectional Warping, effectively combining their advantages. A quantitative comparison between Forward and Bidirectional Warping is provided in Table I.

The Bidirectional Warping process operates in two sequential stages—depth warping followed by image warping—to effectively overcome the limitations of pure Forward Warping. Specifically, the method first warps and interpolates depth values to generate a complete virtual depth map, then performs reverse warping for photometrically consistent color interpolation. This approach yields virtual views with significantly reduced artifacts such as graininess and blurring while maintaining computational efficiency. The overall pipeline is illustrated in Figure 5, and the warping process is formulated as follows:

$$\begin{cases} p_{vir} = K_{vir} \cdot R_{vir} \cdot R_{src}^{-1} \cdot (D_{src} \cdot K_{src}^{-1} \cdot p_{src}), \\ D_{vir}(p_{vir}) = \text{Fill}(\text{Bil}(D_{src}(p_{src}))), \end{cases} \quad (17)$$

$$\begin{cases} p_{src} = K_{src} \cdot R_{src} \cdot R_{vir}^{-1} \cdot (D_{vir} \cdot K_{vir}^{-1} \cdot p_{vir}), \\ I_{vir}(p_{vir}) = \text{Bil}(I_{src}(p_{src})), \end{cases} \quad (18)$$

where  $p_{src}$  and  $p_{vir}$  denote pixels in the real view and the virtual view, respectively,  $D_{vir}$  is the virtual depth map generated through Depth Warping, and  $I_{vir}$  is the synthesized virtual image obtained via Image Warping. The source depth map  $D_{src}$  is estimated using monocular depth estimator, with

scale consistency enforced via least-squares optimization. The  $\text{Fill}(\cdot)$  operator handles hole completion in the warped depth map,  $\text{Bil}(\cdot)$  denotes bilinear sampling.

2) *Scale-Agnostic Monocular Depth Recovery*: Virtual view synthesis relies on accurate depth maps from the real views. The scale and offset of scale-agnostic monocular depth maps are recovered via an iterative least-squares optimization:

$$s', b' = \arg \min_{s, b} \sum_{z \in D_{SP}} \|M_{RC} \odot D_{SP}(z) - D'(s, b)\|_2^2, \quad (19)$$

where  $D'$  is obtained through the linear transformation  $D' = s \cdot D_{mono} + b$ ,  $D_{SP}$  is sparse depth points generated from robust camera-space depths  $z$  obtained through Hybrid-Loss Depth Estimation, and  $M_{RC}$  is the reprojection error mask. The training view's depth map with the recovered scale  $s'$  and offset  $b'$  is given by:

$$D_{src} = s' \cdot D_{mono} + b'. \quad (20)$$

### 3) Virtual View Selection & Fusion: Virtual Pose Selection

**via Pose Scoring:** To generate high-quality virtual views, a scoring function is proposed to prioritize source real views that are geometrically close to the target virtual pose. The Nearest Neighbor Score for each candidate pose is computed based on both translational distance and rotational difference, with higher scores assigned to closer poses with more similar orientations.

**Multi-View Fusion:** Since a virtual view generated from a single source view may contain occlusions or missing regions, a fusion strategy aggregates information from multiple sources. Specifically, the top- $k$  virtual views rendered at the same target pose are fused; these views are generated from source views selected based on the highest pose similarity scores. The view from the closest source serves as a base, while others are blended to expand visible regions. The complete fusion process is formulated as follows:

$$I'_{vir} = \text{Fuse}_k(I_{vir} | \text{Order}(\text{Score}(R_{src}, R_{vir}))). \quad (21)$$

where  $\text{Score}(\cdot)$  denotes the Nearest Neighbor Score quantifying pose similarity,  $\text{Order}(\cdot)$  sorts source poses in descending order based on their  $\text{Score}$  values, indicating their proximity to the target virtual pose,  $\text{Fuse}_k(\cdot)$  represents the operation of fusing the top- $k$  virtual views, and  $I'_{vir}$  is the final fused virtual view. Figure 6 illustrates the fusion result.

The virtual depth map and occlusion mask corresponding to the virtual view are also generated through Bidirectional Warping and the Selection & Fusion operations, as illustrated in Figure 5.

TABLE I  
COMPARISON BETWEEN FORWARD WARPING AND BIDIRECTIONAL  
WARPING METRICS.

Scene	Forward Warping			Bidirectional Warping		
	PSNR↑	SSIM↑	LPIPS↓	PSNR↑	SSIM↑	LPIPS↓
Fern	22.58	0.751	0.175	22.67	0.752	0.175
Leaves	18.07	0.658	0.238	18.14	0.659	0.237
Room	22.43	0.868	0.142	22.53	0.868	0.141

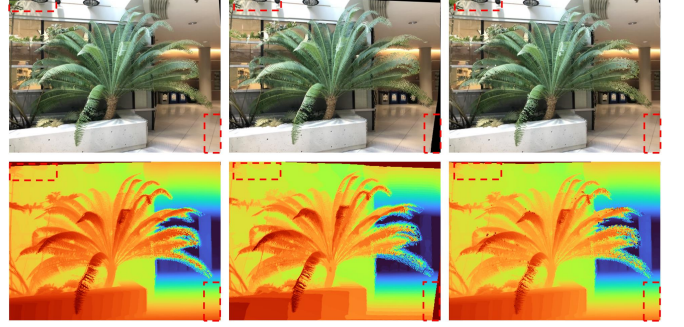


Fig. 6. Multi-View Fusion. Fusing the two left virtual views produces the result shown on the right.

4) *Loss function*: The loss function for virtual view supervision is defined as follows:

$$\begin{cases} L_{grad} = L_1(G(M) \odot G(I_{ren}), G(M) \odot G(I'_{vir})), \\ L_{color}^{vir} = \alpha L_{grad} + \beta L_{ssim}(M \odot I_{ren}, M \odot I'_{vir}), \end{cases} \quad (22)$$

$$L_{depth}^{vir} = \text{PCC}(M \odot D_{ren}, M \odot D_{vir}), \quad (23)$$

where  $M$  is the virtual view mask,  $G(\cdot)$  computes the image gradient domain,  $\alpha$  and  $\beta$  are weighting coefficients satisfying  $\alpha + \beta = 1$ , and  $\text{PCC}(\cdot)$  denotes the Pearson Correlation Coefficient operation. The gradient-domain loss  $L_{grad}$  enhances sensitivity to edges and structural details by emphasizing high-frequency information, while maintaining robustness to absolute intensity variations. The Pearson Correlation Coefficient for depth loss measures linear dependence between rendered and virtual depths, effectively capturing structural consistency while being invariant to global scale shifts.

### E. Occlusion-Aware Reconstruction

In NVS, models are typically optimized to reconstruct only the visible regions present in the training views. However, synthesizing views beyond the original training set often reveals occluded areas, presenting a significant challenge. This issue is exacerbated under sparse-view conditions, where limited coverage increases the probability of exposing unseen regions in novel views.

Regions exhibiting substantial depth differences between foreground and background are particularly prone to occlusions. Based on this, an Occlusion-Aware Reconstruction method grounded in depth differences is proposed, as illustrated in Figure 7. This component is suited for reconstructing smaller occluded regions. First, edge gradients of the depth map are computed using the Sobel operator to extract candidate regions  $a$  with large foreground-background depth disparities. Since such edge regions often fail to form continuous occlusion boundaries, the monocular depth map  $D_{mono}$  is partitioned into  $n$  discrete depth layers. The depth slice  $b$  where pixels from region  $a$  are predominantly distributed is identified to generate an initial foreground mask. To refine the mask and exclude foreground regions with insignificant depth variations, the minimum bounding rectangle  $c$  of region  $a$  is extracted. This rectangle is used to crop content from

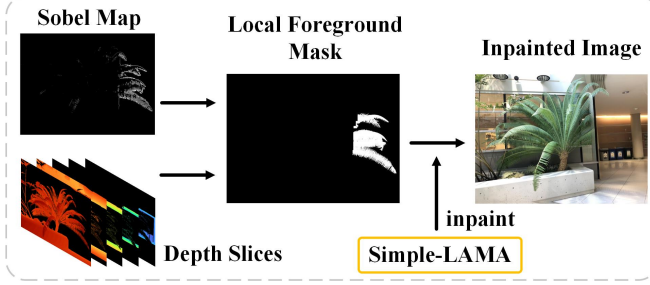


Fig. 7. Occlusion-Aware Reconstruction Pipeline. Local foreground mask, generated by utilizing the sobel map and depth slices, identifies the inpainting regions and guides the Simple-LAMA model to perform the inpainting.

depth slice  $b$ , producing a local foreground mask emphasizing regions with pronounced depth differences:

$$M_{local\_FG} = \mathcal{F}(Sobel(D_{mono}), Slice(D_{mono})). \quad (24)$$

where  $D_{mono}$  denotes the monocular depth map,  $Sobel(\cdot)$  represents the Sobel edge detection operator,  $Slice(\cdot)$  refers to the depth slicing operation, and  $\mathcal{F}$  denotes the function that extracts the local foreground mask  $M_{local\_FG}$ .

The Simple-LAMA [41] inpainting model is subsequently employed to generate plausible completion results. This model uses the  $M_{local\_FG}$  along with the training views as input, where the mask specifically identifies regions that require completion:

$$I_{inp} = Lama(M_{local\_FG}, I), \quad (25)$$

where  $I_{inp}$  denotes the image after inpainting. To enforce geometric consistency and refine the reconstruction, the inpainting image  $I_{inp}$  is used to supervise the background Gaussian splatting process. The background point set is first isolated by filtering out foreground regions using the occlusion-aware mask:

$$P_{BG} = P \odot \neg(M_{local\_FG} \odot M_{D\_slice}), \quad (26)$$

$$S(t) = \begin{cases} Train(I_{inp}, P_{BG}), & \text{if } t \leq t_{BG}, \\ Train(I, P), & \text{if } t > t_{BG} \end{cases} \quad (27)$$

where  $M_{D\_slice}$  is a depth slice mask that identifies regions with depth values less than the current slice threshold,  $P$  denotes the original 3D point cloud, and  $P_{BG}$  represents the point cloud after excluding points in the occluded foreground regions. The background Gaussians are optimized exclusively using  $I_{inp}$  as supervision for the first  $t_{BG}$  iterations, after which the entire set of Gaussians is trained to reconstruct the complete scene. Ablation will demonstrate the effectiveness of the proposed Occlusion-Aware Reconstruction.

#### F. Total Loss Function

The overall optimization objective combines photometric, geometric, and virtual view consistency terms, defined as:

$$L_{col}(I) = \lambda L_1(I_{ren}, I) + (1 - \lambda) L_{ssim}(I_{ren}, I), \quad (28)$$

$$L_{total} = L_{col}(I) + L_{dep}(D) + L_{col}(I_{vir}) + L_{dep}(D_{vir}), \quad (29)$$

where  $L_{dep}(D)$  denotes the depth loss as defined in Eq. 16,  $L_{col}(I_{vir})$  denotes the virtual image color loss as defined in Eq. 22, and  $L_{dep}(D_{vir})$  denotes the virtual depth loss as defined in Eq. 23. The weight  $\lambda$  is set to 0.8 in all experiments.

## IV. EXPERIMENT

### A. Setup

1) *Datasets*: DWGS is evaluated on five widely adopted public datasets: LLFF, IBRNet, Blender, DTU, and Tanks&Temples. These datasets cover forward-facing, synthetic, object-centric, and 360° unbounded scenes, ensuring a comprehensive assessment of robustness across diverse settings. For LLFF and IBRNet (forward-facing scenes), we follow the protocol of DNGaussian [27] and SCGaussian [37]: one every 8 images is held out for testing, while 3 training views are uniformly sampled from the remainder. Evaluation is performed over LLFF scenes with 8x, 4x downsampling rate and IBRNet scenes with 2x downsampling rate. For Blender (synthetic objects), models are trained on 8 views and evaluated on 25 uniformly sampled test images with a 2x downsampling rate. For DTU (object-centric scenes), we adopt the setup from SCGaussian [37], using provided object masks during evaluation to exclude background regions and focus on the target object. A 4x downsampling rate is applied. For Tanks&Temples (360° scenes), 6 scenes are selected. Training uses 24 views, and training and testing split strategy follows the same protocol as used in LLFF (one every 8 images) with 4x downsampling rate.

2) *Evaluation Metrics*: Rendering quality is evaluated using PSNR, SSIM, and LPIPS. In addition, following DNGaussian [27], the Average (AVG) is computed as a composite metric, defined as the geometric mean of MSE ( $10^{-\text{PSNR}/10}$ ),  $\sqrt{1 - \text{SSIM}}$ , and LPIPS. Efficiency is assessed via frames per second (FPS) and total training time. To ensure statistical robustness, each scene is evaluated 7 times. The highest and lowest PSNR values are discarded, and the remaining 5 results are averaged to obtain the scene-level performance. Final dataset-level metrics are reported as the average across all scenes.

3) *Baselines*: DWGS is compared against several excellent sparse-view NVS jobs, including NeRF-based and 3DGS-based approaches. NeRF-based baselines include FreeNeRF [8] and SparseNeRF [7]. 3DGS-based baselines include vanilla 3DGS [5], FSGS [26], SID [39], DNGaussian [27], MCGS [36], and SCGaussian [37]. For NeRF-based methods, we report their best quantitative results from the respective papers. To ensure a fair comparison, we use public code with consistent training-testing splits and a unified base environment with core dependencies fixed, including PyTorch and CUDA.

4) *Implementation Details*: DWGS is built upon the 3DGS framework [5] and implemented in PyTorch. Camera poses are estimated using COLMAP across all views for robustness. To ensure consistent comparison, similar to SCGaussian, we employed the GIM-DKM [42] model for dense matching to extract matching points per training view. Besides, we use ML-depth-pro [43] for monocular depth estimation, which excels in

TABLE II  
QUANTITATIVE COMPARISONS ON THE LLFF (1/8, 1/4 RESOLUTION), IBRNET (1/2 RESOLUTION) DATASETS WITH 3 TRAINING VIEWS. TOP-3 ENTRIES ARE HIGHLIGHTED: RED (1ST), ORANGE (2ND), YELLOW (3RD).

Method	1/8 LLFF				1/4 LLFF				1/8 IBRNet			
	PSNR↑	SSIM↑	LPIPS↓	AVG↓	PSNR↑	SSIM↑	LPIPS↓	AVG↓	PSNR↑	SSIM↑	LPIPS↓	AVG↓
FreeNeRF [8]	19.63	0.612	0.308	0.134	18.73	0.562	0.384	0.169	19.76	0.588	0.333	0.135
SparseNeRF [7]	19.86	0.624	0.328	0.127	19.07	0.564	0.401	0.168	19.90	0.593	0.364	0.137
3DGS [5]	15.42	0.383	0.463	0.218	13.28	0.350	0.486	0.264	17.20	0.556	0.355	0.165
FSGS [26]	20.27	0.697	0.206	0.102	19.70	0.667	0.265	0.117	19.67	0.605	0.306	0.127
SID [39]	20.40	0.701	0.215	0.102	19.08	0.635	0.336	0.135	19.44	0.599	0.360	0.137
DNGaussian [27]	19.12	0.591	0.294	0.132	18.23	0.575	0.386	0.155	18.14	0.554	0.415	0.161
MCGS [36]	20.32	0.700	0.219	0.103	19.63	0.663	0.292	0.122	21.02	0.674	0.282	0.109
SCGaussian [37]	20.73	0.725	0.196	0.095	20.03	0.683	0.266	0.114	21.47	0.689	0.275	0.103
DWGS(Ours)	21.13	0.735	0.189	0.090	20.30	0.693	0.256	0.109	22.19	0.708	0.249	0.093

capturing fine details. Both depth estimation and scene training are iterated 2,000 times, following the configuration of SC-Gaussian [37]. Initialize and generate Gaussian primitives after filtering outliers. Bidirectional Warping generates 50 virtual views; one virtual view iteration is performed for every 5 real view iterations. The Occlusion-Aware Reconstruction applies a depth difference mask to prioritize rendering of occluded region Gaussians in the first 1,000 iterations, followed by training all Gaussians. Gaussian cloning and pruning follow the vanilla 3DGS settings. All experiments are conducted on a single NVIDIA RTX 3090 GPU. For detailed configuration, please refer to the publicly available code.

### B. Comparison

1) *LLFF & IBRNet*: Quantitative results on the LLFF and IBRNet datasets under extremely sparse settings (3 training

views) are summarized in Table II. DWGS achieves state-of-the-art performance, reaching a PSNR of 21.13 dB and LPIPS of 0.189 on LLFF, and 22.19 dB PSNR with 0.249 LPIPS on IBRNet, outperforming all baseline methods across metrics.

Qualitative results are shown in Figures 8 and 9. The GT depth map is obtained from monocular depth estimator. In the Fortress and Horns scenes of LLFF dataset, SID, MCGS, and SCGaussian exhibit various artifacts and detail loss. Although SID preserves depth details better, this comes at the cost of generating more spatial points and longer training time. In the Signboard and Table scenes of IBRNet dataset, methods such as FSGS, DNGaussian, and SCGaussian also suffer from artifacts and a lack of fine details. SCGaussian is particularly prone to artifacts due to insufficient outlier filtering. Moreover, SID, MCGS, FSGS, and DNGaussian all show a common limitation: the loss of fine details in close-range areas and

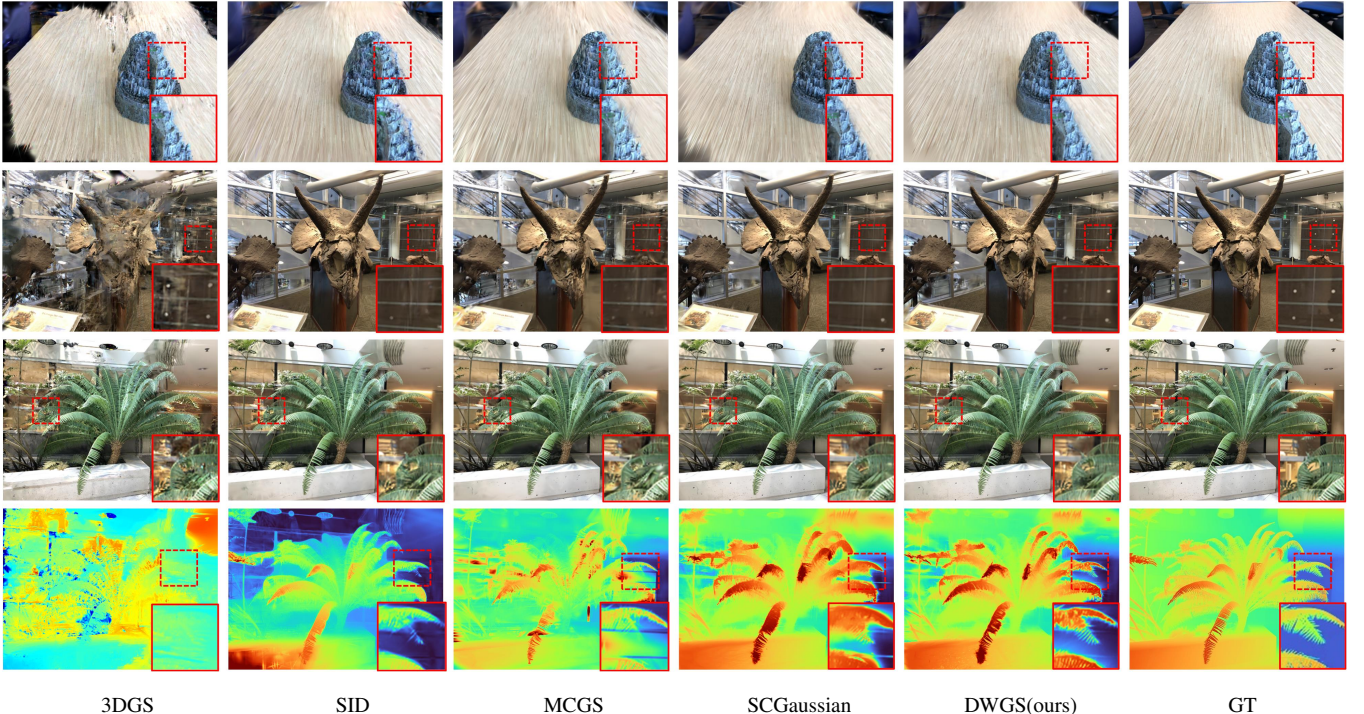


Fig. 8. Qualitative comparison on LLFF dataset under 3 training views. The rendering results of our DWGS are more accurate and display finer details.

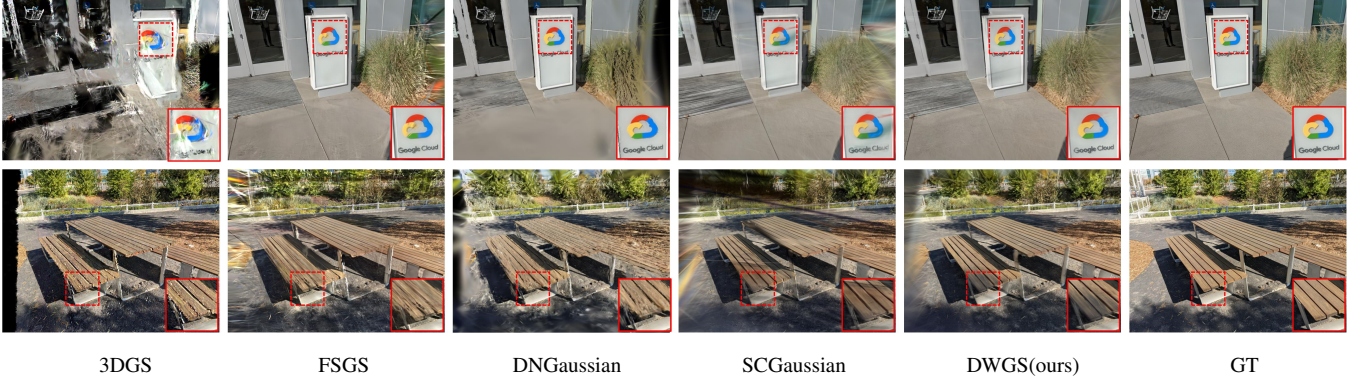


Fig. 9. Qualitative comparison on IBRNet dataset with 3 training views. The rendering results of DWGS method are more accurate and display finer details.

TABLE III

QUANTITATIVE COMPARISONS ON THE BLENDER (1/2 RESOLUTION)  
DATASETS WITH 8 TRAINING VIEWS. TOP-3 ENTRIES ARE HIGHLIGHTED:  
RED (1ST), ORANGE (2ND), YELLOW (3RD).

Method	Blender			
	PSNR $\uparrow$	SSIM $\uparrow$	LPIPS $\downarrow$	AVG $\downarrow$
3DGS [5]	22.85	0.836	0.141	0.066
FSGS [26]	16.35	0.601	0.369	0.175
SID [39]	12.65	0.729	0.321	0.208
DNGaussian [27]	22.79	0.870	0.106	0.058
MCGS [36]	24.06	0.887	0.089	0.048
SCGaussian [37]	23.33	0.883	0.097	0.053
DWGS(Ours)	24.18	0.894	0.086	0.047

the introduction of blur in distant regions.

In contrast, DWGS produces renderings that closely match the GT across all forward-facing scenes, with enhanced edge sharpness, improved texture preservation, and minimal artifacts. These results demonstrate DWGS's robustness and superiority in challenging sparse-view reconstruction of forward-facing scenes.

2) *Blender*: Quantitative comparisons on the Blender dataset with 8 training views are presented in Table III, DWGS achieves the best performance across all metrics.

Qualitative results are shown in Figure 10. In the Chair object, MCGS produces noticeable floaters, while DNGaussian suffers from blurred details. For the Lego object, both MCGS and DNGaussian fail to reconstruct fine structures, leading to a loss of detail. In the Drums and Ship objects, 3DGS and SCGaussian exhibit floaters, with 3DGS showing the most severe floaters as well as a clear color discrepancy from the GT. In contrast, DWGS produces superior reconstruction results and more accurate depth maps, with sharper geometry and better-preserved textures.

3) *DTU*: Quantitative comparisons on the DTU dataset are summarized in Table IV, where DWGS achieves the highest scores across all metrics, followed by SCGaussian and MCGS.

Figure 11 presents the rendering results. Both 3DGS and DNGaussian produce a considerable number of floaters. FSGS and SID fail to reconstruct textual details and suffer from overall blurriness. While MCGS and SCGaussian also exhibit floaters, MCGS shows the most severe cases, which further

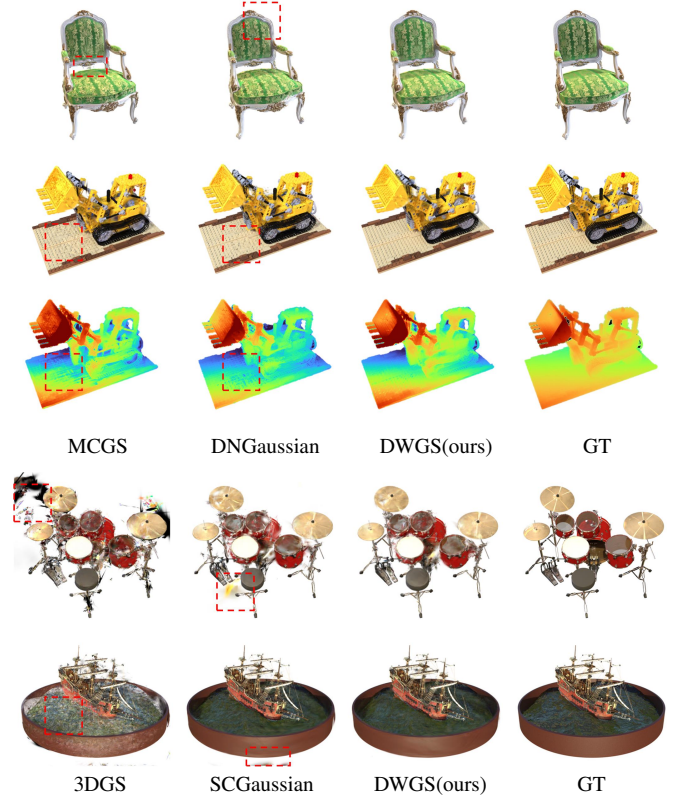


Fig. 10. Qualitative comparison on Blender dataset with 8 training views. DWGS method excels both in geometry and rendering qualities.

lead to inaccurate depth estimations. Benefiting from the outlier filtering mechanism and virtual view constraints, DWGS significantly reduces artifacts and improves texture fidelity, particularly around text and fine structures.

4) *Tanks&Temples*: The Tanks&Temples dataset is employed to evaluate the performance of DWGS in large-scale 360° unbounded scenes. Quantitative results are presented in Table V. Note that evaluations on this dataset utilize only the Hybrid-Loss Depth Estimation component of our framework. DNGaussian and MCGS are excluded from comparison as they lack configurations suitable for 360° unbounded scenes.

Qualitative results are shown in Figure 12. As SID is an enhanced version of FSGS, only FSGS is presented for

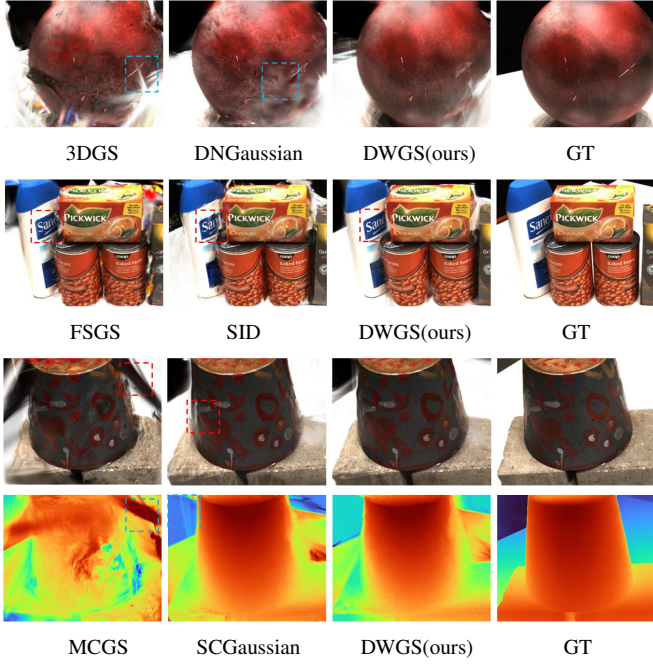


Fig. 11. Qualitative comparison on DTU dataset with 3 training views.

TABLE IV

QUANTITATIVE COMPARISONS ON THE DTU (1/4 RESOLUTION) DATASETS WITH 3 TRAINING VIEWS. TOP-3 ENTRIES ARE HIGHLIGHTED: RED (1ST), ORANGE (2ND), YELLOW (3RD).

Method	DTU			
	PSNR $\uparrow$	SSIM $\uparrow$	LPIPS $\downarrow$	AVG $\downarrow$
FreeNeRF [8]	19.92	0.787	0.182	0.098
SparseNeRF [7]	19.55	0.769	0.201	0.102
3DGS [5]	12.76	0.595	0.376	0.233
FSGS [26]	17.41	0.728	0.247	0.132
SID [26]	16.35	0.654	0.334	0.165
DNGaussian [27]	18.46	0.807	0.168	0.101
MCGS [36]	19.02	0.810	0.154	0.094
SCGaussian [37]	19.11	0.857	0.123	0.082
DWGS(Ours)	20.22	0.872	0.110	0.072

clarity. In the Family and Horse scenes, both vanilla 3DGS and SID exhibit significant artifacts, with the latter also showing noticeable color rendering errors. SCGaussian suffers from partial object omission. In contrast, DWGS produces more complete and geometrically stable reconstructions with reduced artifacts, demonstrating its robustness in challenging large-scale unbounded scenarios.

5) *Efficiency*: The proposed DWGS method matches the efficiency of other advanced approaches, achieving an inference speed of 250 FPS, which is comparable to methods such as SCGaussian and MCGaussian, while maintaining a low average training time of 2.5 minutes. In terms of GPU memory usage, DWGS optimizes resource consumption, requiring 3 GB for the Hybrid-Loss Depth Estimation (HLDE) component and 5 GB for the Virtual View Synthesis (VVS) component, outperforming methods like FreeNeRF (4x48 GB) and SparseNeRF (32 GB). Compared to approaches such as 3DGS (7.5 minutes, 2 GB) and FSGS (17 minutes, 3 GB),

TABLE V  
QUANTITATIVE COMPARISONS ON THE TANK&TEMPLE (1/4 RESOLUTION) DATASETS WITH 24 TRAINING VIEWS. TOP-3 ENTRIES ARE HIGHLIGHTED: RED (1ST), ORANGE (2ND), YELLOW (3RD).

Method	Tank&Temple			
	PSNR $\uparrow$	SSIM $\uparrow$	LPIPS $\downarrow$	AVG $\downarrow$
3DGS [5]	18.77	0.706	0.267	0.124
FSGS [26]	19.39	0.720	0.273	0.118
SID [26]	19.51	0.723	0.273	0.117
SCGaussian [37]	18.96	0.722	0.298	0.125
DWGS(Ours)	20.00	0.749	0.268	0.110

TABLE VI  
EFFICIENCY COMPARISON OF DIFFERENT METHODS.

Method	Inference (FPS)	Average training time	GPU Mem
FreeNeRF [8]	$9 \times 10^{-2}$	2.3 h	4x48 GB
SparseNeRF [7]	$9 \times 10^{-2}$	1.5 h	32 GB
3DGS [5]	400	7.5 min	2 GB
FSGS [26]	300	17 min	3 GB
SID [26]	300	28 min	3.5 GB
DNGaussian [27]	500	3.5 min	2 GB
MCGS [36]	250	2.5 min	2 GB
SCGaussian [37]	250	1.5 min	3 GB
DWGS	250	2.5 min	3 GB (HLDE) 5 GB (VVS)

DWGS offers a substantial reduction in training time while preserving real-time inference capabilities, making it a highly efficient solution for practical 3D reconstruction tasks.

### C. Ablation

An ablation study is conducted on the LLFF dataset under a 3-view setting to evaluate the individual contributions of the core components in DWGS: Hybrid-Loss Depth Estimation (HLDE), Bidirectional Warping Virtual View Synthesis (VVS), and Occlusion-Aware Reconstruction (OAR). Quantitative results are summarized in Table VII. The baseline methods, vanilla 3DGS and SCGaussian, achieve a PSNR of 15.42 dB and 20.73 dB, respectively, with LPIPS scores of 0.463 and 0.196. The combination of HLDE + VVS + OAR (full DWGS) yields the best performance, achieving a PSNR of 21.13 dB and an LPIPS of 0.189.

Figure 13 provides a qualitative comparison of different component configurations on the Fern scene. In the boxed regions, the following observations are made: +HLDE: Produces more robust depth estimates, effectively resolving structural distortions present in 3DGS. +VVS: Introduces virtual view constraints, significantly reducing artifacts and improving consistency. +OAR: Generates more plausible background content and alleviates occlusion-related artifacts.

Compared to the baseline methods, DWGS produces renderings that are visually closer to the ground truth, demonstrating the effectiveness of the proposed components.

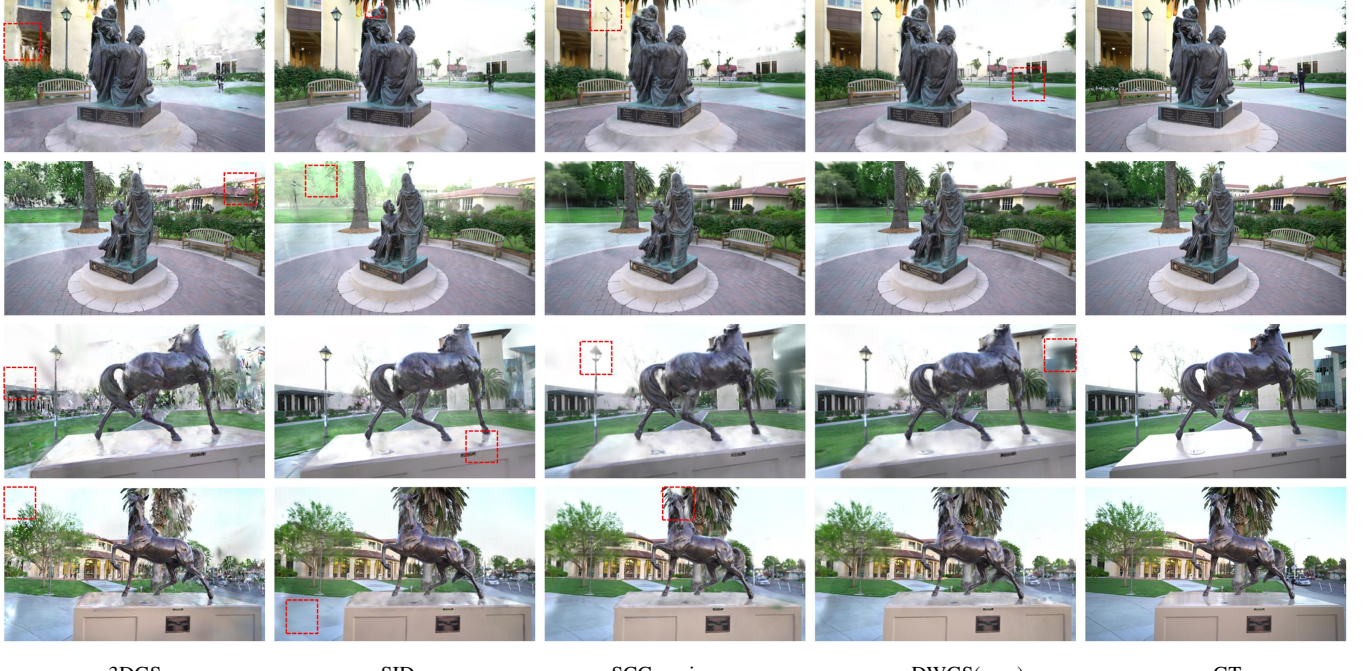


Fig. 12. Qualitative comparison on Tank&Temple dataset with 24 training views. DWGS method excels both in geometry and rendering qualities in difficult areas.

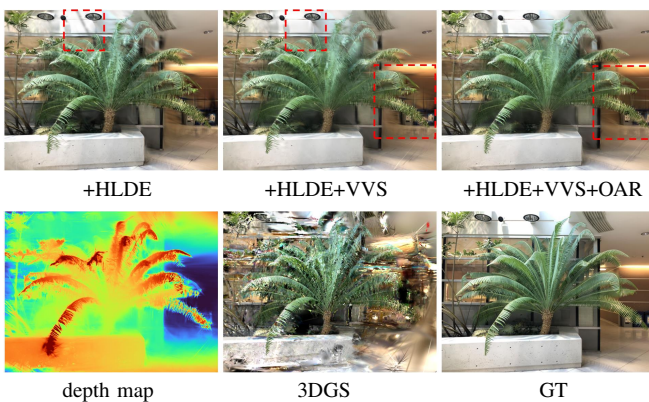


Fig. 13. Ablation study on component contributions. Compared to 3DGS, the rendering results of full DWGS model are closest to GT.

TABLE VII  
ABLATION STUDY ON THE COMPONENTS OF DWGS.

Method	HLDE	VVS	OAR	PSNR↑	SSIM↑	LPIPS↓	AVG↓
3DGS	✗	✗	✗	15.42	0.383	0.463	0.221
SCG	✗	✗	✗	20.73	0.725	0.196	0.100
DWGS (Ours)	✓	✗	✗	20.91	0.732	0.187	0.097
	✗	✓	✗	20.93	0.731	0.191	0.098
	✗	✗	✓	20.85	0.727	0.191	0.099
	✓	✓	✗	21.11	0.734	0.191	0.096
	✓	✓	✓	21.13	0.735	0.189	0.096

## V. CONCLUSION

**Limitations:** DWGS relies on COLMAP for pose estimation and uses fixed thresholds in its propagation constraints. The occlusion handling module is currently optimized for foreground content and may not generalize well to sky or homogeneous regions. DWGS is tailored for static scenes and does not support dynamic content.

**Conclusion:** This paper presents DWGS, an effective framework for sparse-view NVS based on 3DGS. The core of our approach includes three innovations: a Hybrid-Loss Depth Estimation module that enforces multi-view consistency through reprojection and point propagation constraints; a Bidirectional Warping Virtual View Synthesis method that enhances the coverage of unobserved regions, thereby mitigating overfitting to the limited input views; and an Occlusion-Aware Reconstruction component that improves background rendering through depth-difference priors. Extensive experiments across standard benchmarks demonstrate that DWGS achieves state-of-the-art performance under extreme sparsity. We believe our work offers a valuable step toward practical and high-quality 3D reconstruction from very few images.

## REFERENCES

- [1] X. Tu, L. Radl, M. Steiner, M. Steinberger, B. Kerbl, and F. de la Torre, “Vrsplat: Fast and robust gaussian splatting for virtual reality,” *Proceedings of the ACM on Computer Graphics and Interactive Techniques*, vol. 8, no. 1, p. 1–22, May 2025.
- [2] S. Dasgupta, A. Gupta, S. Tuli, and R. Paul, “Actnerf: Uncertainty-aware active learning of nerf-based object models for robot manipulators using visual and re-orientation actions,” in *2024 IEEE/RSJ International Conference on Intelligent Robots and Systems (IROS)*. IEEE, Oct. 2024, p. 13062–13069.

[3] X. Zhou, Z. Lin, X. Shan, Y. Wang, D. Sun, and M.-H. Yang, “Drivinggaussian: Composite gaussian splatting for surrounding dynamic autonomous driving scenes,” in *2024 IEEE/CVF Conference on Computer Vision and Pattern Recognition (CVPR)*. IEEE, Jun. 2024, p. 21634–21643.

[4] B. Mildenhall, P. P. Srinivasan, M. Tancik, J. T. Barron, R. Ramamoorthi, and R. Ng, “Nerf: representing scenes as neural radiance fields for view synthesis,” *Communications of the ACM*, vol. 65, no. 1, p. 99–106, Dec. 2021.

[5] B. Kerbl, G. Kopanas, T. Leimkuhler, and G. Drettakis, “3d gaussian splatting for real-time radiance field rendering,” *ACM Transactions on Graphics*, vol. 42, no. 4, p. 1–14, Jul. 2023.

[6] A. Jain, M. Tancik, and P. Abbeel, “Putting nerf on a diet: Semantically consistent few-shot view synthesis,” in *2021 IEEE/CVF International Conference on Computer Vision (ICCV)*. IEEE, Oct. 2021, p. 5865–5874.

[7] G. Wang, Z. Chen, C. C. Loy, and Z. Liu, “Sparsenerf: Distilling depth ranking for few-shot novel view synthesis,” in *2023 IEEE/CVF International Conference on Computer Vision (ICCV)*. IEEE, Oct. 2023.

[8] J. Yang, M. Pavone, and Y. Wang, “Freenerf: Improving few-shot neural rendering with free frequency regularization,” in *2023 IEEE/CVF Conference on Computer Vision and Pattern Recognition (CVPR)*. IEEE, Jun. 2023, p. 8254–8263.

[9] H. Xiong, S. Muttukuru, H. Xiao, R. Upadhyay, P. Chari, Y. Zhao, and A. Kadambi, “Sparsegs: Sparse view synthesis using 3d gaussian splatting,” in *2025 International Conference on 3D Vision (3DV)*. IEEE, Mar. 2025, p. 1032–1041.

[10] C. Yang, S. Li, J. Fang, R. Liang, L. Xie, X. Zhang, W. Shen, and Q. Tian, “Gaussianobject: High-quality 3d object reconstruction from four views with gaussian splatting,” *ACM Transactions on Graphics*, vol. 43, no. 6, p. 1–13, Nov. 2024.

[11] J. Chung, J. Oh, and K. M. Lee, “Depth-regularized optimization for 3d gaussian splatting in few-shot images,” in *Proceedings of the IEEE/CVF Conference on Computer Vision and Pattern Recognition*, 2024, pp. 811–820.

[12] J. T. Barron, B. Mildenhall, M. Tancik, P. Hedman, R. Martin-Brualla, and P. P. Srinivasan, “Mip-nerf: A multiscale representation for anti-aliasing neural radiance fields,” in *2021 IEEE/CVF International Conference on Computer Vision (ICCV)*. IEEE, Oct. 2021.

[13] J. T. Barron, B. Mildenhall, D. Verbin, P. P. Srinivasan, and P. Hedman, “Mip-nerf 360: Unbounded anti-aliased neural radiance fields,” in *2022 IEEE/CVF Conference on Computer Vision and Pattern Recognition (CVPR)*. IEEE, Jun. 2022.

[14] T. Müller, A. Evans, C. Schied, and A. Keller, “Instant neural graphics primitives with a multiresolution hash encoding,” *ACM Transactions on Graphics*, vol. 41, no. 4, p. 1–15, Jul. 2022.

[15] M. Niemeyer, J. T. Barron, B. Mildenhall, M. S. M. Sajjadi, A. Geiger, and N. Radwan, “Regnerf: Regularizing neural radiance fields for view synthesis from sparse inputs,” in *2022 IEEE/CVF Conference on Computer Vision and Pattern Recognition (CVPR)*. IEEE, Jun. 2022.

[16] A. Radford, J. W. Kim, C. Hallacy, A. Ramesh, G. Goh, S. Agarwal, G. Sastry, A. Askell, P. Mishkin, J. Clark *et al.*, “Learning transferable visual models from natural language supervision,” in *International conference on machine learning*. PMLR, 2021, pp. 8748–8763.

[17] N. Somraj and R. Soundararajan, “Vip-nerf: Visibility prior for sparse input neural radiance fields,” in *Special Interest Group on Computer Graphics and Interactive Techniques Conference Conference Proceedings*, ser. SIGGRAPH ’23. ACM, Jul. 2023, p. 1–11.

[18] R. Wu, B. Mildenhall, P. Henzler, K. Park, R. Gao, D. Watson, P. P. Srinivasan, D. Verbin, J. T. Barron, B. Poole, and A. Hołyński, “Reconfusion: 3d reconstruction with diffusion priors,” in *2024 IEEE/CVF Conference on Computer Vision and Pattern Recognition (CVPR)*. IEEE, Jun. 2024, p. 21551–21561.

[19] L. Yen-Chen, P. Florence, J. T. Barron, A. Rodriguez, P. Isola, and T.-Y. Lin, “Inerf: Inverting neural radiance fields for pose estimation,” in *2021 IEEE/RSJ International Conference on Intelligent Robots and Systems (IROS)*. IEEE, Sep. 2021.

[20] Z. Wang, S. Wu, W. Xie, M. Chen, and V. A. Prisacariu, “Nerf–: Neural radiance fields without known camera parameters,” 2021.

[21] C.-H. Lin, W.-C. Ma, A. Torralba, and S. Lucey, “Barf: Bundle-adjusting neural radiance fields,” in *2021 IEEE/CVF International Conference on Computer Vision (ICCV)*. IEEE, Oct. 2021, p. 5721–5731.

[22] J. Tang, J. Ren, H. Zhou, Z. Liu, and G. Zeng, “Dreamgaussian: Generative gaussian splatting for efficient 3d content creation,” *arXiv preprint arXiv:2309.16653*, 2023.

[23] T. Yi, J. Fang, J. Wang, G. Wu, L. Xie, X. Zhang, W. Liu, Q. Tian, and X. Wang, “Gaussiandreamer: Fast generation from text to 3d gaussians by bridging 2d and 3d diffusion models,” in *2024 IEEE/CVF Conference on Computer Vision and Pattern Recognition (CVPR)*. IEEE, Jun. 2024, p. 6796–6807.

[24] J. Luiten, G. Kopanas, B. Leibe, and D. Ramanan, “Dynamic 3d gaussians: Tracking by persistent dynamic view synthesis,” in *2024 International Conference on 3D Vision (3DV)*. IEEE, Mar. 2024, p. 800–809.

[25] G. Wu, T. Yi, J. Fang, L. Xie, X. Zhang, W. Wei, W. Liu, Q. Tian, and X. Wang, “4d gaussian splatting for real-time dynamic scene rendering,” in *2024 IEEE/CVF Conference on Computer Vision and Pattern Recognition (CVPR)*. IEEE, Jun. 2024, p. 20310–20320.

[26] Z. Zhu, Z. Fan, Y. Jiang, and Z. Wang, “Fsgs: Real-time few-shot view synthesis using gaussian splatting,” in *European conference on computer vision*. Springer, 2024, pp. 145–163.

[27] J. Li, J. Zhang, X. Bai, J. Zheng, X. Ning, J. Zhou, and L. Gu, “Dngaussian: Optimizing sparse-view 3d gaussian radiance fields with global-local depth normalization,” in *2024 IEEE/CVF Conference on Computer Vision and Pattern Recognition (CVPR)*. IEEE, Jun. 2024, p. 20775–20785.

[28] A. Paliwal, W. Ye, J. Xiong, D. Kotovenko, R. Ranjan, V. Chandra, and N. K. Kalantari, “Coherentgs: Sparse novel view synthesis with coherent 3d gaussians,” in *European Conference on Computer Vision*. Springer, 2024, pp. 19–37.

[29] J. Zhang, J. Li, X. Yu, L. Huang, L. Gu, J. Zheng, and X. Bai, *CoR-GS: Sparse-View 3D Gaussian Splatting via Co-regularization*. Springer Nature Switzerland, Sep. 2024, p. 335–352.

[30] H. Yu, X. Long, and P. Tan, “Lm-gaussian: Boost sparse-view 3d gaussian splatting with large model priors,” *arXiv preprint arXiv:2409.03456*, 2024.

[31] B. Ke, K. Qu, T. Wang, N. Metzger, S. Huang, B. Li, A. Obukhov, and K. Schindler, “Marigold: Affordable adaptation of diffusion-based image generators for image analysis,” *IEEE Transactions on Pattern Analysis and Machine Intelligence*, p. 1–18, 2025.

[32] L. Zhang, A. Rao, and M. Agrawala, “Adding conditional control to text-to-image diffusion models,” in *Proceedings of the IEEE/CVF international conference on computer vision*, 2023, pp. 3836–3847.

[33] W. Xu, H. Gao, S. Shen, R. Peng, J. Jiao, and R. Wang, *MVPGS: Excavating Multi-view Priors for Gaussian Splatting from Sparse Input Views*. Springer Nature Switzerland, Nov. 2024, p. 203–220.

[34] Y. Yao, Z. Luo, S. Li, T. Fang, and L. Quan, *MVSNet: Depth Inference for Unstructured Multi-view Stereo*. Springer International Publishing, 2018, p. 785–801.

[35] A. Beyer and L. Alexy, “An image equals 16x16 words: Scaling image recognition with transformers,” 2025.

[36] Y. Xiao, D. Zhai, W. Zhao, K. Jiang, J. Jiang, and X. Liu, “Mcgs: Multiview consistency enhancement for sparse-view 3d gaussian radiance fields,” *arXiv preprint arXiv:2410.11394*, 2024.

[37] R. Peng, W. Xu, L. Tang, J. Jiao, R. Wang *et al.*, “Structure consistent gaussian splatting with matching prior for few-shot novel view synthesis,” *Advances in Neural Information Processing Systems*, vol. 37, pp. 97 328–97 352, 2024.

[38] L. Han, J. Zhou, Y.-S. Liu, and Z. Han, “Binocular-guided 3d gaussian splatting with view consistency for sparse view synthesis,” *Advances in Neural Information Processing Systems*, vol. 37, pp. 68 595–68 621, 2024.

[39] Z. He, Z. Xiao, K.-C. Chan, Y. Zuo, J. Xiao, and K.-M. Lam, “See in detail: Enhancing sparse-view 3d gaussian splatting with local depth and semantic regularization,” *arXiv preprint arXiv:2501.11508*, 2025.

[40] M. Caron, H. Touvron, I. Misra, H. Jégou, J. Mairal, P. Bojanowski, and A. Joulin, “Emerging properties in self-supervised vision transformers,” in *Proceedings of the International Conference on Computer Vision (ICCV)*, 2021.

[41] R. Suvorov, E. Logacheva, A. Mashikhin, A. Remizova, A. Ashukha, A. Silvestrov, N. Kong, H. Goka, K. Park, and V. Lempitsky, “Resolution-robust large mask inpainting with fourier convolutions,” *arXiv preprint arXiv:2109.07161*, 2021.

[42] X. Shen, Z. Cai, W. Yin, M. Müller, Z. Li, K. Wang, X. Chen, and C. Wang, “Gim: Learning generalizable image matcher from internet videos,” in *The Twelfth International Conference on Learning Representations*, 2024.

[43] A. Bochkovskii, A. Delaunoy, H. Germain, M. Santos, Y. Zhou, S. R. Richter, and V. Koltun, “Depth pro: Sharp monocular metric depth in less than a second,” in *International Conference on Learning Representations*, 2025.

TABLE VIII  
QUANTITATIVE COMPARISONS ON THE LLFF DATASET WITH 2,3,5 TRAINING VIEWS. THE BEST, SECOND-BEST ENTRIES ARE MARKED IN RED, ORANGE.

Scene	Method	2-view				3-view				5-view			
		PSNR $\uparrow$	SSIM $\uparrow$	LPIPS $\downarrow$	AVG $\downarrow$	PSNR $\uparrow$	SSIM $\uparrow$	LPIPS $\downarrow$	AVG $\downarrow$	PSNR $\uparrow$	SSIM $\uparrow$	LPIPS $\downarrow$	AVG $\downarrow$
Fern	3DGS	14.07	0.306	0.509	0.255	15.80	0.348	0.502	0.220	25.02	0.647	0.255	0.078
	SCG	19.38	0.627	0.317	0.133	22.15	0.741	0.175	0.084	24.20	0.824	0.120	0.057
	DWGS	<b>20.09</b>	<b>0.658</b>	<b>0.258</b>	<b>0.115</b>	<b>22.73</b>	<b>0.753</b>	<b>0.173</b>	<b>0.078</b>	<b>24.52</b>	<b>0.832</b>	<b>0.110</b>	<b>0.054</b>
Flower	3DGS	16.15	0.370	0.437	0.203	16.37	0.445	0.437	0.195	26.10	0.782	0.146	0.055
	SCG	19.84	0.608	0.307	0.134	21.66	0.690	<b>0.217</b>	0.103	25.86	0.858	0.097	0.045
	DWGS	<b>20.10</b>	<b>0.630</b>	<b>0.274</b>	<b>0.126</b>	<b>21.70</b>	<b>0.693</b>	0.221	<b>0.104</b>	<b>25.96</b>	<b>0.861</b>	<b>0.090</b>	<b>0.044</b>
Fortress	3DGS	15.70	0.325	0.379	0.203	18.80	0.437	0.367	0.153	23.74	0.613	0.229	0.084
	SCG	21.34	0.558	0.294	0.114	25.00	0.823	0.122	0.056	27.48	0.867	0.094	0.040
	DWGS	<b>22.17</b>	<b>0.646</b>	<b>0.274</b>	<b>0.097</b>	<b>25.68</b>	<b>0.836</b>	<b>0.117</b>	<b>0.051</b>	<b>27.60</b>	<b>0.871</b>	<b>0.093</b>	<b>0.039</b>
Horns	3DGS	14.35	0.291	0.511	0.250	15.65	0.391	0.463	0.214	19.07	0.528	0.359	0.145
	SCG	16.84	0.554	0.372	0.176	19.86	0.737	0.221	0.109	22.71	0.821	0.158	0.077
	DWGS	<b>17.76</b>	<b>0.624</b>	<b>0.319</b>	<b>0.152</b>	<b>20.33</b>	<b>0.746</b>	<b>0.219</b>	<b>0.105</b>	<b>23.38</b>	<b>0.832</b>	<b>0.145</b>	<b>0.070</b>
Leaves	3DGS	13.18	0.249	0.452	0.266	14.94	0.342	0.410	0.220	18.20	0.528	0.300	0.145
	SCG	15.30	0.419	0.454	0.216	17.97	0.651	0.240	0.131	19.46	0.720	0.203	0.106
	DWGS	<b>15.86</b>	<b>0.482</b>	<b>0.396</b>	<b>0.192</b>	<b>18.14</b>	<b>0.659</b>	<b>0.237</b>	<b>0.128</b>	<b>19.70</b>	<b>0.734</b>	<b>0.194</b>	<b>0.102</b>
Orchids	3DGS	14.88	0.214	0.492	0.242	15.95	0.313	0.460	0.213	20.21	0.472	0.340	0.132
	SCG	14.40	0.384	0.363	0.218	16.43	0.530	0.248	0.157	17.93	0.619	0.203	0.126
	DWGS	<b>14.63</b>	<b>0.414</b>	<b>0.328</b>	<b>0.205</b>	<b>16.67</b>	<b>0.543</b>	<b>0.234</b>	<b>0.150</b>	<b>17.83</b>	<b>0.617</b>	<b>0.202</b>	<b>0.127</b>
Room	3DGS	12.09	0.326	0.581	0.308	13.51	0.451	0.546	0.262	16.23	0.451	0.508	0.207
	SCG	19.87	0.793	0.228	0.104	22.12	0.858	0.150	0.071	26.20	0.910	0.107	0.045
	DWGS	<b>20.75</b>	<b>0.823</b>	<b>0.190</b>	<b>0.089</b>	<b>22.53</b>	<b>0.868</b>	<b>0.141</b>	<b>0.066</b>	<b>26.64</b>	<b>0.915</b>	<b>0.103</b>	<b>0.043</b>
Trex	3DGS	11.20	0.225	0.552	0.332	12.35	0.344	0.518	0.290	14.67	0.436	0.436	0.223
	SCG	18.40	0.665	0.291	0.138	20.62	0.774	0.193	0.093	23.24	0.851	0.132	0.063
	DWGS	<b>19.35</b>	<b>0.702</b>	<b>0.236</b>	<b>0.115</b>	<b>21.27</b>	<b>0.787</b>	<b>0.171</b>	<b>0.084</b>	<b>24.01</b>	<b>0.864</b>	<b>0.120</b>	<b>0.057</b>
Mean	3DGS	13.95	0.288	0.489	0.255	15.42	0.383	0.463	0.218	20.41	0.557	0.322	0.124
	SCG	<b>18.17</b>	<b>0.576</b>	<b>0.328</b>	<b>0.148</b>	<b>20.73</b>	<b>0.725</b>	<b>0.196</b>	<b>0.095</b>	<b>23.38</b>	<b>0.809</b>	<b>0.139</b>	<b>0.065</b>
	DWGS	<b>18.84</b>	<b>0.622</b>	<b>0.280</b>	<b>0.131</b>	<b>21.13</b>	<b>0.735</b>	<b>0.189</b>	<b>0.090</b>	<b>23.71</b>	<b>0.816</b>	<b>0.133</b>	<b>0.062</b>

## APPENDIX

### A. Detailed contract experiments

Table VIII presents the detailed experimental results on the LLFF dataset, trained with 2, 3, and 5 images, comparing the 3DGS, SCG, and DWGS methods. It is evident that the DWGS method achieves the best evaluation results across different numbers of images. Notably, training with 2 images does not utilize Point Propagation Constraints (PPC).

### Algorithm 1 Point Propagation Constraint (PPC)

**Input:** Matching point pairs  $\mathcal{M}_{i,j} = \{(\mathbf{p}_i^a, \mathbf{p}_j^b)\}$  between views  $i$  and  $j$ ,  $\mathcal{M}_{j,k} = \{(\mathbf{p}_j^b, \mathbf{p}_k^c)\}$  between views  $j$  and  $k$ , pixel distance threshold  $\epsilon$ ;

**Output:** Common point set  $\mathcal{C} = \{(\mathbf{p}_i^a, \mathbf{p}_k^c)\}$  for indirect matching between views  $i$  and  $k$ ;

1: **Construct KD-Tree for View  $j$ :**

2: Merge all  $\mathbf{p}_j^b$  from  $\mathcal{M}_{i,j}$  and  $\mathbf{p}_j^b$  from  $\mathcal{M}_{j,k}$  into set  $\mathcal{P}_j$

3: Build KD-Tree  $\mathcal{T}_j$  using  $\mathcal{P}_j$

4: **Search for Nearest Neighbor Pairs:**

5: Initialize empty set  $\mathcal{C}$

6: **for** each  $\mathbf{p}_j^b \in \mathcal{M}_{i,j}$  **do**

7:     Find nearest neighbor  $\mathbf{p}_j^{b'}$  in  $\mathcal{T}_j$

8:     **if**  $\|\mathbf{p}_j^b - \mathbf{p}_j^{b'}\|_2 < \epsilon$  **then**

9:         Extract corresponding  $\mathbf{p}_i^a$  from  $\mathcal{M}_{i,j}$  and  $\mathbf{p}_k^c$  from  $\mathcal{M}_{j,k}$

10:         Add  $(\mathbf{p}_i^a, \mathbf{p}_k^c)$  to  $\mathcal{C}$

11:     **end if**

12: **end for**

13: **return**  $\mathcal{C}$

### B. PPC with different numbers of common point sets

By using different nearest neighbor distances, different point propagation common point sets can be obtained. Figure 14 shows the line graph of PSNR values versus nearest neighbor distance. It can be observed that as the nearest neighbor distance increases, both the number of common points and the PSNR value gradually rise. However, when the distance exceeds 3, the PSNR for both the Fern scene and the LLFF dataset begins to decline. The point (22.38, 99) represents the PSNR value and the number of common points for the Fern scene, respectively. Notably, if the number of common points is less than 100 following a secondary filtering step, the PPC operation is skipped to avoid redundant processing.

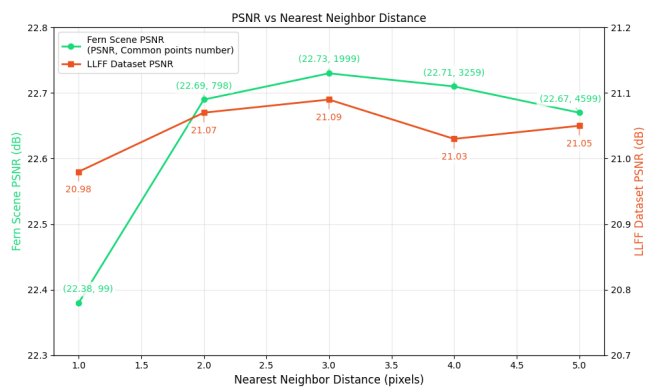


Fig. 14. PSNR vs Nearest Neighbor Distance.